

Characterization of Water-Based Anti-Corrosion and Anti-Fouling Coating in the Heat Exchanger Tube of Gas Water Heater

Lei WANG¹, Lijun WU^{1*}, Zhicheng YUAN¹, Xingyuan LIANG¹, Wenzheng CHEN²

¹ School of Mechanical Engineering, Tongji University, Shanghai 201804, PR China

² Sichuan Luheng Energy Technology Co., Mianyang 621000, PR China

<http://doi.org/10.5755/j02.ms.34613>

Received 3 July 2023; accepted 8 January 2024

Due to the fouling and corrosion issues with gas water heater heat exchangers during use, a water-based coating is created using the sol-gel method and applied to the inner surface of the copper tube of the heat exchangers. The water-based coating can reduce the surface energy of copper that is oxygen-free by 82.40 % and has outstanding hydrophobicity. The coating's adhesion strength was 8.46 MPa, and its wet adhesion reduction rate was only 0.0375 MPa·d⁻¹ when submerged in a bath of water at a constant temperature. Its water contact angle remained above 110° even after being abraded by sandpaper, demonstrating its excellent wear resistance. At a constant temperature of 45 °C, the corrosion experiment was carried out in salt, acid, and alkali solutions. The maximum corrosion rate of the coating was $3.24 \times 10^{-2} \text{mg} \cdot (\text{cm}^2 \cdot \text{h})^{-1}$, which was only 20.85 % of that of the oxygen-free copper substrate. The dynamic fouling experiment shows that the coating can effectively inhibit fouling growth, prolong the fouling induction period and reduce the average fouling rate. By factoring in the fouling thermal resistance and the coating thermal resistance, the overall heat transfer coefficient of the copper tube was computed. The results demonstrate that after applying this water-based coating, the copper tube can continue to have a high heat transfer coefficient for an extended period, ensuring the continuous and effective operation of the heat exchanger and having practical application value.

Keywords: gas water heater, water-based coating, anti-corrosion, anti-fouling, heat transfer analysis.

1. INTRODUCTION

Gas water heaters are becoming increasingly popular as a means of supplying hot water to residential and commercial users as human living conditions and the need for comfort increase [1, 2]. Due to the easy fouling and corrosive ions, such as Ca²⁺, Mg²⁺, Cl⁻, HCO₃⁻, and SO₄²⁻, that are present in large quantities in the water during usage, the heat exchanger, which is the main component of gas water heaters, is subject to the "threat" of fouling and corrosion [3, 4]. What is more deadly is that fouling and corrosion often occur together, with fouling accelerating the corrosion of copper pipes and corrosion leading to rapid deposition of scale in the pipes. As the loose scale layer can retain oxygen and corrosive ions, these corrosive media further accelerate the local corrosion of copper pipes; at the same time, the products generated by corrosion lead to an increase in the surface roughness of copper pipes, thus providing suitable growth sites for deposited salt crystals and increasing the probability of fouling [5]. Therefore, fouling and corrosion lead to the thinning of the effective thickness of copper tubes, which destroys the internal metallurgical organization of oxygen-free copper, leading to a decrease in the mechanical properties and pressure-bearing capacity of heat exchangers, significantly shortening their service life while causing serious losses and significant threats to the safety of human life and property [6].

To solve the above problems, a variety of anti-corrosion

and scale inhibition methods have been studied, such as changing the metal composition [7], controlling the corrosive environment [8], electrochemical protection [9], coating protection [10, 11], etc. Among them, the advantages of coating protection technology have attracted extensive attention from researchers. The studies of Qing and Jiang show that the surface of superhydrophobic coating has significant anti-corrosion and scale-inhibiting properties [12, 13]. Many scholars prepare superhydrophobic coating on the surface of the copper substrate, usually using chemical, electrochemical, or physical methods. First, the surface is etched to form a rough surface microstructure. The rough surface is then modified with low surface energy substances such as thiols and fluorinated silanes to obtain a superhydrophobic surface [14, 15]. However, not all superhydrophobic surfaces have higher corrosion and scale inhibition performance than hydrophobic surfaces. Yu et al. prepared several hydrophobic and superhydrophobic composite coatings and found that the corrosion rate of the samples with superhydrophobic performance was higher than that of the other samples [16], which was because the rough structure of superhydrophobic surfaces happened to provide invasion channels for the corrosive medium of small molecules, and the corrosion rate of the superhydrophobic surfaces increased instead, as compared to the surfaces that did not achieve superhydrophobic effect. Oliveira found that if the roughness is too large, the surface will form a strong mechanical occlusion with the dirt, and the high roughness can also promote scaling by blocking the

* Corresponding author. Tel.: +86-13917547917.

E-mail: ljwu@tongji.edu.cn (L. Wu)

fluid shear force for the dirt particles [17]. In addition, the superhydrophobic coating preparation process is relatively complex, the microstructure durability is poor, and the raw material is easy to cause environmental pollution, and cannot meet the environmental requirements of gas water heaters. Therefore, it is still difficult for superhydrophobic coatings to meet the application requirements of long-lasting anti-corrosion and scale inhibition for heat exchangers [18, 19]. To provide long-lasting protection for heat exchanger and to reduce scale deposition on the inner surface of copper tubes, the preparation of new and efficient anticorrosive, scale inhibiting and environmentally friendly coating is essential.

In this paper, a water-based, environmentally friendly long-lasting, corrosion-resistant, and anti-fouling coating was prepared by sol-gel method using modified silica, graphite, silicon carbide, and graphene as fillers and aqueous silicone modified resin and aqueous silicone emulsion as solvents. The basis for reducing the surface energy of the coating was discussed by analyzing the wetting performance of the coating, and the mechanical strength characteristics of the coating were further tested to judge its durability in practical application. The study of corrosion and fouling behavior of coating in harsh environments was carried out to provide theoretical references for practical applications. Finally, the advantages of the coating in the practical application were illustrated by analyzing the effects of fouling and coating on the heat transfer performance of copper tubes.

2. EXPERIMENT

2.1. Material surface preparation

Three material surface samples were prepared: polished oxygen-free copper surface, denoted by OC; pure aqueous silicone resin coating on the oxygen-free copper surface, denoted by OC-WSR; and aqueous silicone resin-inorganic filler composite coating on the oxygen-free copper surface, denoted by OC-WSR-IF. The following briefly describes the preparation process of these three kinds of samples and the sample preparation process is shown in Fig. 1.

1. OC sample: First, the surface of oxygen-free copper was initially cleaned with metal cleaner, and then the surface was polished and polished with files and sandpaper; then, it was ultrasonically cleaned with ethanol and distilled water for 5 minutes, respectively. Finally, the surface was dried to produce the OC sample.
2. OC-WSR sample: First, a mixture of water-based silicone-modified resin and water-based silicone

emulsion was configured in the ratio of 3:1.7 and sprayed on the polished and cleaned oxygen-free copper substrate. After spraying, the OC-WSR sample was dried naturally at room temperature for 10 hours, heated to 130 °C for 30 minutes in an electric blast dryer, and finally cooled to room temperature.

3. OC-WSR-IF sample: First, 2 wt.% modified silica (average particle size: 20 nm), 2 wt.% silicon carbide, 3 wt.% graphite, and 0.1 wt.% multilayer graphene (average particle size: 5 μm) were mixed into inorganic filler, and the inorganic filler was uniformly dispersed in the mixture prepared in (2) by magnetic stirring and ultrasonic dispersion. Then, the OC-WSR-IF sample was prepared according to the steps in (2).

2.2. Sample surface energy analysis

Surface energy is an intrinsic property of coating, and coating with low surface energy has good hydrophobic effects while providing excellent results in reducing the deposition of hydrophilic fouling. Therefore, the magnitude of the surface energy of a coating is critical to the deposition rate of fouling [20, 21]. Among the surface energy determination methods, the contact angle method is widely considered to be the most direct and effective.

2.2.1. Surface wettability

Wettability is one of the critical properties of a solid surface. Solid surfaces are wetted during solid-liquid contact, which is usually characterized by the contact angle (CA) or rolling angle (SA); in the case of solid surfaces, if $CA < 90^\circ$, they are hydrophilic and more easily wetted by liquids; if $CA > 90^\circ$, they are hydrophobic and less easily wetted by liquids [22]. The static contact angles of different standard liquids (distilled water and ethylene glycol) on the sample surfaces were measured using a contact angle measuring instrument (ASR-705B, Guangdong Aisry Instrument Technology Co., Ltd.). Five different locations were selected on the sample's surface for each group of tests, and the results were averaged.

2.2.2. Surface energy calculation

For solid surfaces, the surface energy is more difficult to obtain by direct measurement methods due to the existence of microscopic scratches, pits, and other unevenness on the surface, and the surface environment is very complex, so the solid surface energy is often obtained by indirect calculation of the solid surface energy based on experiments. Therefore, the three samples' surface energy was calculated using the contact angle method developed by Owens and Wendt [23].

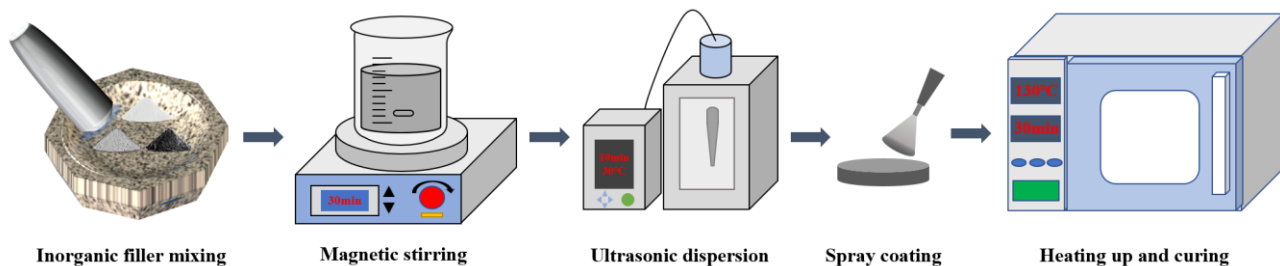


Fig. 1. Schematic diagram of the sample preparation process

The essence of solid surface wetting is that the liquid is attached by the action of the adhesion force on the solid surface. The work of adhesion W_a can be expressed as:

$$W_a = \gamma_{LV}(1 + \cos\theta), \quad (1)$$

where γ_{LV} is the free energy per unit area of the liquid-gas interface; θ is the static contact angle. Owens and Wendt considered that the work of adhesion consists of the dispersion component and the polar component, so the work of adhesion can also be written as:

$$W_a = 2\sqrt{\gamma_{SV}^d\gamma_{LV}^d} + 2\sqrt{\gamma_{SV}^p\gamma_{LV}^p}, \quad (2)$$

where γ_{SV}^d and γ_{LV}^d are the dispersive parts of the solid and liquid surface energies; γ_{SV}^p and γ_{LV}^p are the polar parts of the solid and liquid surface energies. From Eq. 1 and Eq. 2, it is obtained that:

$$\gamma_{LV}(1 + \cos\theta) = 2\sqrt{\gamma_{SV}^d\gamma_{LV}^d} + 2\sqrt{\gamma_{SV}^p\gamma_{LV}^p}. \quad (3)$$

For a known standard liquid, the dispersion and polarity components are known, and the unknowns are only γ_{SV}^d and γ_{SV}^p . By measuring the static contact angle between the two standard liquids and the sample surface, the two solid surface energy components in Eq. 3 are solved jointly. The sum of the two γ_{SV} is the surface energy of the sample. The surface energy parameters of distilled water and ethylene glycol are listed in Table 1.

Table 1. Surface energy parameters of standard liquids (20 °C, $\text{mJ}\cdot\text{m}^{-2}$)

Standard liquids	γ_{LV}	γ_{LV}^d	γ_{LV}^p
Distilled water	72.8	21.8	51.0
Ethylene glycol	48.3	29.3	19.0

2.3. Sample mechanical strength characterization

2.3.1. Wet adhesion test

Wet adhesion is the adhesion force measured after the coating absorbs water, and the wet adhesion of the coating is one of the critical factors determining the failure of the coating. If the lateral pressure generated by water at the interface is stronger than the wet adhesion of the coating, the water phase will penetrate laterally and cause the coating to peel off, making the protective function of the coating ineffective; on the contrary, the lateral movement of the water phase is blocked and can only accumulate at the original position, and the stronger wet adhesion of the coating can effectively prevent the water from damaging the coating, making the coating protective function excellent. Considering the working environment of the heat exchanger, the test samples were immersed in a constant temperature water bath at temperatures of $(45 \pm 0.5)^\circ\text{C}$ and $(60 \pm 0.5)^\circ\text{C}$, respectively, and were removed at specific intervals, rinsed with deionized water, and quickly blotted dry with filter paper to determine the wet adhesion of the coating according to ISO 4624:2002 Paints and varnishes – Pull-off test for adhesion.

2.3.2. Abrasion resistance test

The friction resistance of the sample coating surface can be reflected by the excellent hydrophobicity of the coating

even after it is damaged by friction on the sandpaper, as shown in Fig. 2. The surface of the sample coating was placed face down on 400 g metallographic sandpaper, and a 100 g weight was applied to the other side of the sample, which was then moved forward and backward by 10 cm at a constant speed, recorded as one friction resistance cycle. The contact angle of a water droplet on the sample coating surface was measured under different numbers of friction-resistant cycles. The numerical change of the contact angle reflects the friction resistance of the sample coating surface.

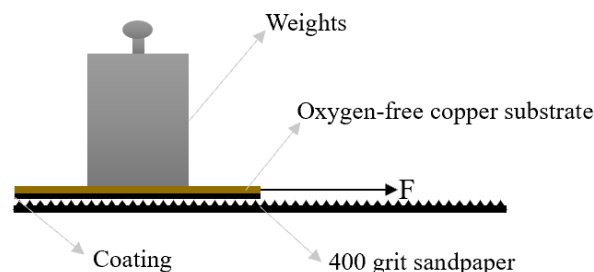


Fig. 2. Diagram of friction resistance test

2.4. Corrosion resistance test

Referring to the ASTM NACE/ASTMG31-12a standard, the immersion method is selected to test the corrosion resistance of the sample coating. Set the corrosion temperature at $(45 \pm 0.5)^\circ\text{C}$ and $(60 \pm 0.5)^\circ\text{C}$; corrosion media were 5 % sulfuric acid, 5 % hydrochloric acid, 5 % sodium hydroxide, and 25 % sodium chloride. The corrosion rate was measured according to the change in weight of the sample before and after corrosion. The selected sample was cylindrical, 30 mm in diameter, 1mm in height, immersed in the corrosion solution before weighing each sample with an analytical balance, every 48 h removed after cleaning and drying weighing records and then replaced by a new corrosion solution for the experiment. Corrosion solution with a beaker and water bath heating to maintain a constant temperature of $(45 \pm 0.5)^\circ\text{C}$ and $(60 \pm 0.5)^\circ\text{C}$.

2.5. Anti-fouling performance test

The samples were suspended in calcium carbonate fouling solution at $(45 \pm 0.5)^\circ\text{C}$ and $(60 \pm 0.5)^\circ\text{C}$ for anti-fouling performance test. CaCO_3 fouling solution was obtained by dissolving a certain amount of NaHCO_3 and anhydrous CaCl_2 in deionized water and preheated to 45°C and 60°C . The fouling solution was put into the rotating hanging tester, the speed was set to 60 r/min, and the prepared sample was hung vertically for the dynamic fouling test. The fouling rate was measured by the weighing method after the samples were rotated and immersed in the fouling solution for a period of time.

3. RESULTS AND DISCUSSION

3.1. Sample surface characterization

Table 2 shows the static contact angles of the three sample surfaces when distilled water and ethylene glycol are used as standard liquids. The results showed that the water contact angle θ_1 and the glycol contact angle θ_2 of the two sample coatings were both hydrophobic and larger than

those of the uncoated surface, indicating that the coating had changed the wetting characteristics of the original surface.

Table 2. The static contact angle of the sample

Sample	Distilled water contact angle θ_1 , °	Ethylene glycol contact angle θ_2 , °
OC	90.4±2.3	59.8±3.4
OC-WSR	102.6±1.2	80.7±1.6
OC-WSR-IF	122.3±1.3	109.6±1.7

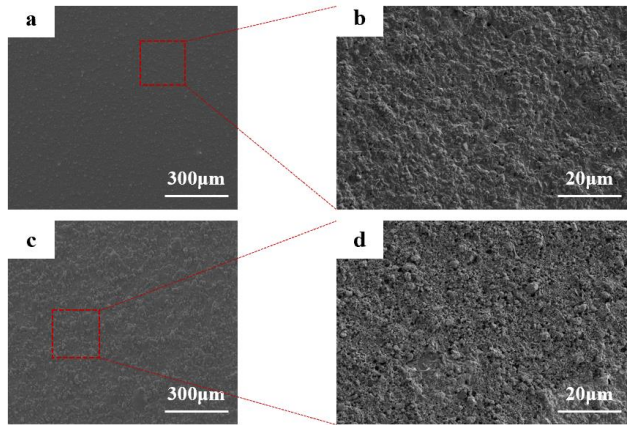


Fig. 3. SEM images of the sample surface: a, b – OC-WSR; c, d – OC-WSR-IF

The surface micromorphology of the coated samples OC-WSR and OC-WSR-IF is shown in Fig. 3. After the addition of modified SiO₂ and other inorganic fillers, the granular projections of the coatings increase, and when the surface is wetted by water, the voids between the projections prevent water from contacting the surface due to the entrainment of air trapped so that water cannot spread on the surface. Therefore, the OC-WSR-IF sample has good hydrophobicity.

The results of the surface energy calculations for the three samples are shown in Table 3. The polished OC sample had the highest surface energy. Because the solid surface energy is defined based on the reversible work done when adding new atoms to the solid surface to establish a new surface, the polished OC sample is a metal surface and off-domain electrons maintain the action force between metal atoms, the magnitude of the action force is almost equal to the chemical bond, the action force is large, the action force field in which the surface atoms are located is more inhomogeneous, and the surface energy is higher. The OC-WSR sample was sprayed with a water-based coating on the polished OC substrate, and the surface energy was reduced. Because the water-based silicone emulsion is an aqueous emulsion of polydimethylsiloxane (PDMS). PDMS, as a hydrophobic polymer, has low surface energy, and its addition to the coating solution can effectively improve the surface energy of the OC-WSR sample. The OC-WSR-IF

Table 3. Surface energy parameters of the samples

Sample	γ_{SV}^d , mJ·m ⁻²	γ_{SV}^p , mJ·m ⁻²	γ_{SV} , mJ·m ⁻²	Rate of change, %
OC	30.84 ± 2.3	2.05 ± 0.2	32.89 ± 2.5	/
OC-WSR	17.37 ± 0.6	1.59 ± 0.12	18.96 ± 0.72	42.35 ± 2.21
OC-WSR-IF	4.95 ± 0.33	0.84 ± 0.06	5.79 ± 0.39	82.40 ± 0.15

Note: Rate of change = (OC surface energy - coating surface energy) / OC surface energy

sample had the lowest surface energy. Compared with the OC sample, the surface energy was reduced by about 82 %. By adding modified SiO₂ and other inorganic fillers and dispersing them uniformly in the coating solution, the surface energy of the coating can be further reduced by building micro-nano rough structures on the coating surface.

3.2. Mechanical strength properties

In the coating preparation process, besides the basic mechanical strength properties determined by the aqueous base resin, the filler's type and content will impact the coating's strength properties. It was found that the addition of silicon carbide (SiC) and graphite (C) to the coating, the synergistic effect of the two, can make the coating have better strength properties. To investigate the distribution ratio of the optimal comprehensive performance when the two components were added to the coating, three sets of comparison experiments were set up, in which the mass ratios of SiC:C were 3:2, 1:1, and 2:3, respectively, under the premise that the sum of the masses of silicon carbide and graphite was 5 wt.%.

Fig. 4 shows the results of the wet adhesion test for different samples. With the increase in soaking time, the wet adhesion on the surface of the OC-WSR sample decreased significantly with a rate of 0.1425 MPa·d⁻¹. This is because the resin contains more hydroxyl groups, which makes the water quickly pass through the coating to the coating/metal interface, resulting in a rapid decrease of the wet adhesion of the coating.

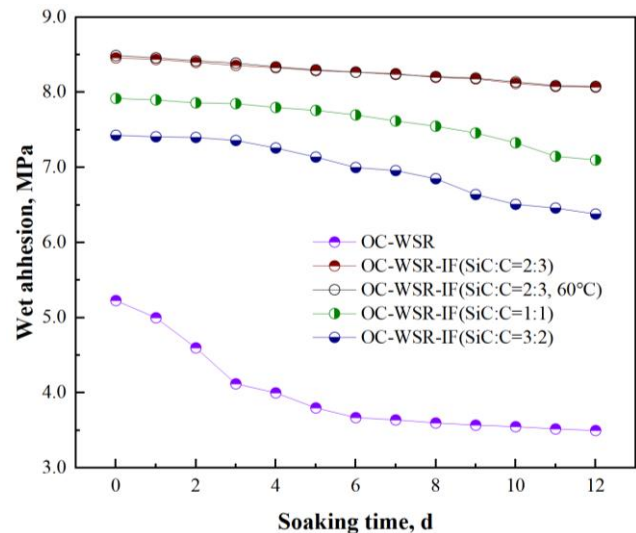


Fig. 4. Variation of sample wet adhesion with soaking time

By adding inorganic filler, the resin can be fully wetted and wrapped with fill to enhance the denseness of the coating, which can effectively prevent the penetration of water, oxygen, and ions and slow down the rate of reduction of wet adhesion of the coating.

When the mass ratio of SiC:C was 2:3, the wet adhesion of the coating was relatively the highest, and the reduction rate was only $0.0375 \text{ MPa}\cdot\text{d}^{-1}$ and the wet adhesion of the samples did not show significant changes after the experimental temperature was increased. The main reason is that graphite is a layered material, and the surface area of graphite is larger, which can increase the contact area with resin and increase the mutual adsorption between them, and then improve the adhesion strength of the coating.

The durability of hydrophobic coatings is often reflected by their abrasion resistance. Fig. 5 shows the variation pattern of the contact angle of the OC-WSR and OC-WSR-IF sample surfaces after sandpaper friction. Due to the sandpaper friction, the roughness of the sample surface at different locations was different, and the contact angle was measured at different points after a certain number of friction-resistant cycles. Therefore, the contact angle of the sample surface fluctuated with the increase in the number of friction-resistant cycles. From the overall results, the contact angle of the sample surface decreased as the number of friction-resistant cycles increased. The OC-WSR sample showed a rapid decrease in contact angle during the friction resistance cycle, and the surface changed from hydrophobic to hydrophilic, while the contact angle of the OC-WSR-IF sample was $> 110^\circ$ after 1000 friction resistant cycles and still maintained good hydrophobicity. The main reason is that silicon carbide is a hard, wear-resistant filler, which can effectively carry external forces, and the relatively high content of graphite can prevent the coating from being damaged by a larger contact area between the two when the coating is subjected to external cyclic reciprocal frictional forces. With the synergistic effect of graphite and silicon carbide, the OC-WSR-IF sample exhibits good mechanical stability and can withstand the damage of certain external forces with good wear resistance.

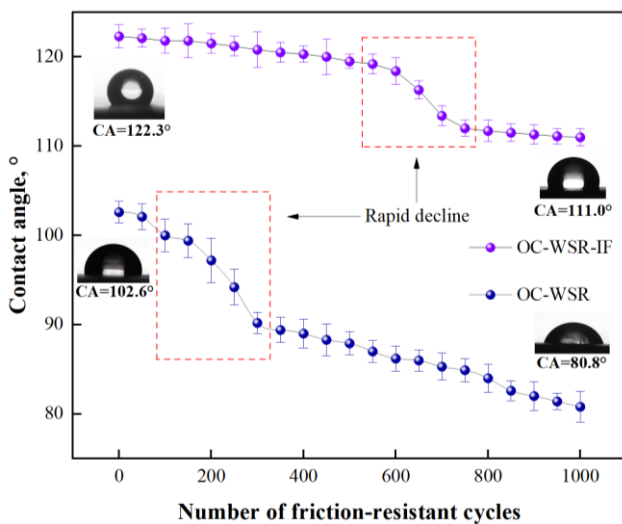


Fig. 5. Variation of contact angle of the sample surface with the number of friction-resistant cycles

The wear resistance mechanism of the coating under the synergistic effect of graphite and silicon carbide is explored, as shown in Fig. 6. When graphite and silicon carbide are added to the coating, fine cracks can be generated on the coating surface when it is subjected to reciprocal friction,

which may cause the surface coating to spill. As the number of friction-resistant cycles increases, the cracks generated on the surface of the coating begin to expand to the inside of the coating, and when the cracks expand to the vicinity of the graphite, the easy slippage of the graphite plays a slowing role in the expansion of the cracks, i.e., it increases the crack expansion path. At the same time, the silicon carbide and the coating have a high internal bonding force, which will not easily peel off from the inside of the coating, playing a good role in bearing the external force mass. Therefore, the synergistic effect of graphite and silicon carbide makes the coating have good wear resistance performance.

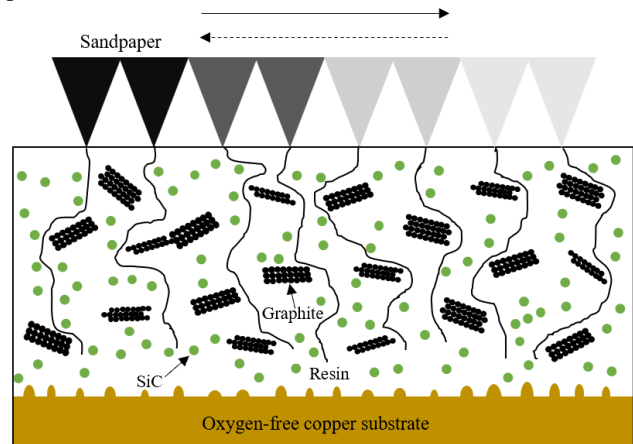


Fig. 6. The wear mechanism of the coating

3.3. Anti-corrosion and anti-fouling properties

The corrosion resistance and anti-fouling performance can measure the coating's ability to protect the heat exchanger and determine whether there is the possibility of contaminating water quality in practical applications. Fig. 7 shows the corrosion rates and contact angles of the three samples after 100 days of immersion in different etching solutions, where the corrosion rate of the OC-WSR-IF sample in 60°C etching solution was measured after 20 days of immersion. The mass loss of the three samples in the sulfuric acid solution was the largest, in which the corrosion rate of OC samples was $15.54 \times 10^{-2} \text{ mg}\cdot(\text{cm}^2\cdot\text{h})^{-1}$. The oxygen-free copper substrate was wholly exposed to the corrosion solution, and pitting occurred in contact with corrosive ions, with more uneven defects appearing on the surface and a rapid decrease in contact angle. The corrosion rate of the OC-WSR sample was $9.49 \times 10^{-2} \text{ mg}\cdot(\text{cm}^2\cdot\text{h})^{-1}$, which was about 40 % lower relative to the OC sample, indicating that the coating could shield the corrosive solution invasion. However, with the extension of the immersion time, due to the poor hydrophobicity of the sample surface, the corrosive solution tends to spread on the surface, pitting of corrosive ions due to capillary action along the coating microcrack defects into the bottom of the coating, destroying of the microstructure of the coating surface, the microcrack further deepen, so that it loses its hydrophobicity. The corrosion rate of the OC-WSR-IF sample was further reduced by adding inorganic filler to the coating, which was only 20.85 % of that of the OC sample, and the coating still had good hydrophobicity after being corroded, showing the relatively best resistance to sulfuric

acid corrosion. The reason is that the OC-WSR-IF sample has low surface energy. The air trapped inside makes it difficult for the corrosive solution to penetrate the microstructure of the coating and not easily contact the surface due to the excellent hydrophobicity and micro-nano structured voids; according to Laplace's equation, the curved liquid surface generates an additional pressure directed toward the corrosive solution, and this additional pressure causes the corrosive solution to be squeezed and drained away, preventing its invasion by corrosive ions [24]. In addition, the inorganic filler is uniformly distributed in the coating by ultrasonic dispersion, which can divide the coating into many small spaces and effectively improve the internal stress concentration of the coating. The filler will form an overlapping "labyrinth" like structure, which can make the corrosive ion infiltration tortuous, thus increasing its diffusion to the substrate. The corrosion rate of the three samples in the rest of the corrosive solution was the same as the sulfuric acid corrosive solution, the corrosion rate of the OC-WSR-IF sample in the hydrochloric acid corrosive solution was 27.15 % of the OC sample, and the corrosion rate in the sodium hydroxide corrosive solution was 21.06 % of OC sample. Therefore, the OC-WSR-IF sample shows the best overall corrosion resistance, however, as the temperature of the corrosive solution increased, the corrosion of the sample surface showed an accelerated trend, the main reason is that as the temperature increases, the diffusion rate of the corrosive ions in the solution increases, and it is easier to penetrate the coating to reach the metal substrate to produce corrosion.

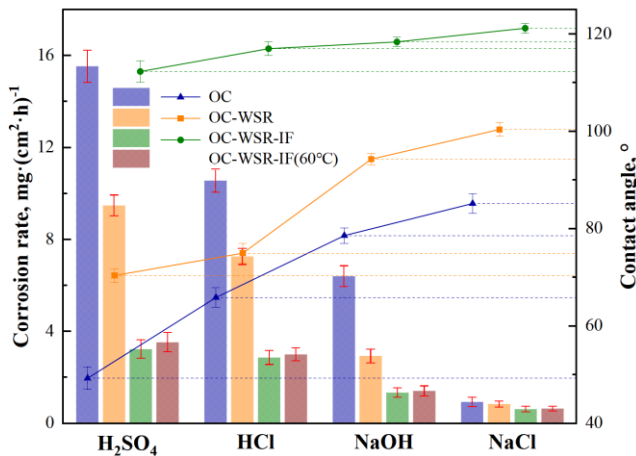


Fig. 7. The corrosion rate of samples in the corrosion solution and the contact angle after being corroded

With the extension of fouling time, the fouling amount of the three samples shows a dynamic increasing trend, as shown in Fig. 8. The whole growth process of the calcium carbonate scale on the surface of the OC sample can be divided into three stages. In the first stage (0 ~ 84 h), the CaCO_3 fouling amount was $0.14 \text{ mg}\cdot\text{cm}^{-2}$, and the average fouling rate was $0.0017 \text{ mg}\cdot(\text{cm}^2\cdot\text{h})^{-1}$, which was equivalent to a period of "dirt-free," i.e., fouling induction period. In the second stage (84 h ~ 240 h), the average fouling rate was $0.0344 \text{ mg}\cdot(\text{cm}^2\cdot\text{h})^{-1}$, CaCO_3 fouling entered the rapid growth period. In the third stage (240 h ~ 492 h), the CaCO_3 fouling amount was almost unchanged relative to the second stage, which was $5.49 \text{ mg}\cdot\text{cm}^{-2}$. The reason is that the

nucleation sites of CaCO_3 on the surface of the OC sample gradually decrease with the increase of fouling time.

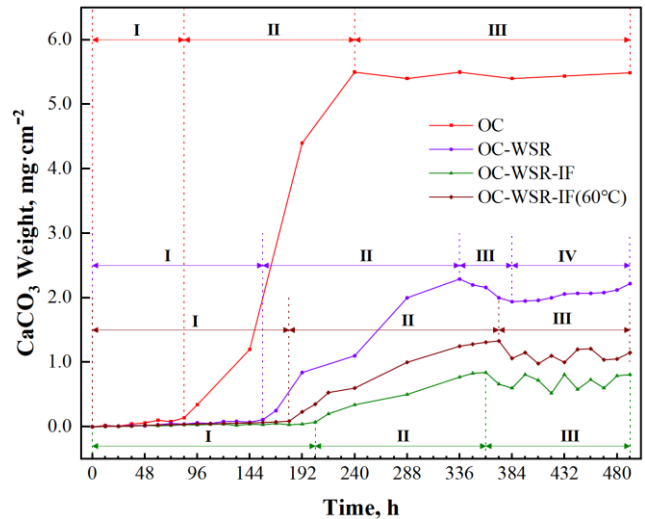


Fig. 8. Variation of sample fouling amount with time

The whole growth process of the calcium carbonate scale on the surface of the OC-WSR sample can be divided into four stages. In the first stage (0 ~ 156 h), the fouling induction period was prolonged nearly two times compared with OC samples. Because the surface energy of the OC-WSR sample is lower and the adhesion between the surface and external substances is weaker. Thus, the dirt is less likely to adhere to the surface. In the second stage (156 h ~ 336 h), the CaCO_3 fouling increased from $0.11 \text{ mg}\cdot\text{cm}^{-2}$ to $2.29 \text{ mg}\cdot\text{cm}^{-2}$, and the average fouling rate was $0.0121 \text{ mg}\cdot(\text{cm}^2\cdot\text{h})^{-1}$, which was 35.17 % of the OC sample. In the third stage (336 h ~ 384 h), the CaCO_3 fouling showed a decreasing trend, and the average fouling rate was $-0.0073 \text{ mg}\cdot(\text{cm}^2\cdot\text{h})^{-1}$, indicating that the scale on the surface of the sample had undergone clearly detached. For the formed fouling layer, the interaction force between them is weaker due to the low surface energy of the sample, and it is easier to flake off from the surface due to impact. In the fourth stage (384 h ~ 492 h), the CaCO_3 fouling amount increased from $1.94 \text{ mg}\cdot\text{cm}^{-2}$ to $2.22 \text{ mg}\cdot\text{cm}^{-2}$ with an average fouling rate of $0.0026 \text{ mg}\cdot(\text{cm}^2\cdot\text{h})^{-1}$, and the surface fouling amount of the sample showed another increasing trend compared with the previous stage. The OC-WSR sample fouling experiment shows that there is a dynamic process of fouling detachment during the whole fouling process of CaCO_3 growth.

The whole growth process of the calcium carbonate scale on the surface of the OC-WSR-IF sample can be divided into three stages. In the first stage (0 ~ 204 h), the fouling induction period lasted longer compared to the OC-WSR sample, which was 2.43 times longer than that of the OC sample, indicating that the fouling induction period has a decreasing relationship with the surface energy. When the temperature of the fouling solution increased, the fouling induction period was shortened, and the rapid growth period of the calcium carbonate scale was advanced to 180 h. In the second stage (204 h ~ 360 h), CaCO_3 fouling increased from $0.07 \text{ mg}\cdot\text{cm}^{-2}$ to $0.84 \text{ mg}\cdot\text{cm}^{-2}$, and the average fouling rate was $0.0049 \text{ mg}\cdot(\text{cm}^2\cdot\text{h})^{-1}$, which was 14.24 % of the OC sample. As the temperature of the fouling solution rose, the

amount of CaCO_3 fouling increased, once the solubility of CaCO_3 decreases with increasing temperature, leading to an increase in precipitation fouling. In the third stage (360 h ~ 492 h), the average fouling rate was significantly reduced to $0.0003 \text{ mg}\cdot(\text{cm}^2\cdot\text{h})^{-1}$ relative to the previous stage. In this stage, the fouling amount of CaCO_3 was dynamically changing. Because the vortex and shear force formed when the fluid flowed over the sample surface has a direct effect on both the fouling rate and the desorption rate of the crystals, due to the effect of fluid shear force, the CaCO_3 crystals adhered to the sample surface are dislodged, and the amount of fouling shows an apparent irregular variation [25]. After 492 h dynamic fouling experiment, the ratio of fouling induction period time of the three samples was 1:1.86:2.43, the ratio of the maximum fouling amount of CaCO_3 was 6.25:2.60:1, and the ratio of average fouling rate in the growth period was 7.02:2.47:1. Therefore, the OC-WSR-IF sample has an excellent anti-fouling performance.

For the application of the coating in the oxygen-free copper tube of the heat exchanger, the anti-fouling mechanism of the coating, combined with the above analysis, is shown in Fig. 9. Firstly, during the flow of water in the copper tube, the positively charged (Ca^{2+} , Mg^{2+}) scale-forming ions and negatively charged (HCO_3^-) scale-forming ions contained in the water collide with each other to form ion pairs and gradually form tiny aggregates after many times of aggregation and dissolution; after that, crystal embryos are formed with these aggregates as the center [26]. Most of the crystal embryos are in an unstable dynamic exchange equilibrium, and some may continue to grow, while others may split into smaller particles or redissolve; until the nuclei become large enough to crystallize and precipitate from the solution; then, the irreversible crystal growth process begins. Due to the presence of a micro-nano

multi-level structure on the coating surface, air can be trapped, and an air film is formed on the coating surface, which effectively prolongs the fouling induction period [27]. After the fouling induction period, accompanied by the destruction of the air film at localized locations on the coating surface, the solid-liquid contact area between the fouling ions in water and the coating is increased, but overall, only a small number of nucleation sites exist on the coating surface, and the amount of fouling is low. In addition, due to the lower surface free energy, lower adhesion work, and non-polarity of the coating, it is not easy for the dirt to be adsorbed on the surface of the coating, and along with the gravitational effect and scouring of the water, the dirt can easily fall off from the surface of the coating, which effectively inhibits the process of dirt formation and growth.

3.4. Heat transfer analysis

Most researchers engage in coating development and fouling research focus on the fouling inhibition effect of the modified surface while ignoring the fact that low surface energy coating materials are mostly organic polymers with their low thermal conductivity. This means that a certain amount of uniform "fouling" has grown inside the tube before fouling has occurred. Therefore, the key to measuring whether the coating can be applied in engineering practice is whether it improves the overall heat transfer performance of oxygen-free copper tubes after fouling. Dirt thermal resistance indicates the value of the degree of heat transfer efficiency reduction due to deposits on the heat exchange surface, that is, the heat transfer resistance caused by deposits on the heat exchange surface, including scale, rust and corrosion, and other additional thermal resistance caused by dirt, of which scale is the main component of the heat exchanger copper tube fouling.

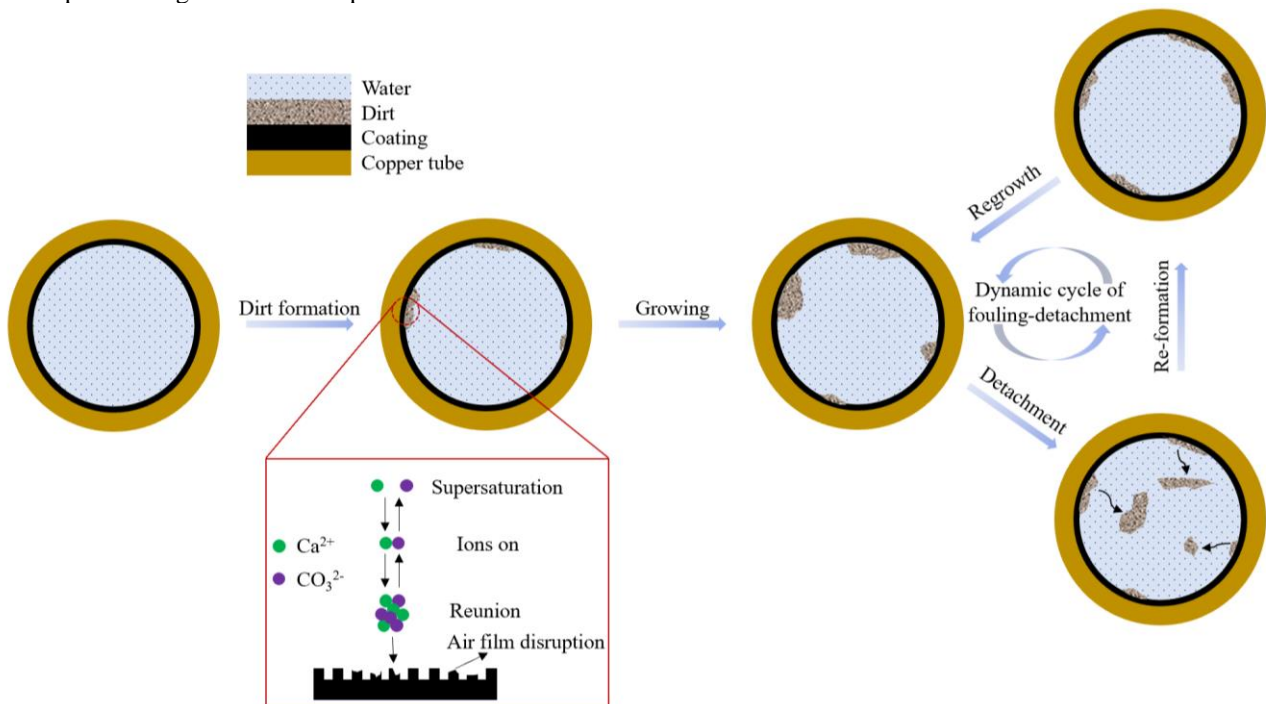


Fig. 9. Anti-fouling mechanism of the inner coating of oxygen-free copper tube

The fouling thermal resistance R_f can be obtained according to equation (4).

$$R_f = \frac{d_{of}}{2\lambda_f} \ln \frac{d_{of}}{d_{if}} \approx \frac{\delta_f}{\lambda_f}, \quad (4)$$

where d_{of} , d_{if} are the outer and inner diameter of the dirt layer, m; λ_f is the thermal conductivity of the dirt, $W \cdot (m \cdot K)^{-1}$; δ_f is the thickness of the dirt layer, m.

The thermal resistance R_t of coating as a special "dirt" is calculated in the same way as the thermal resistance R_f of dirt. $401 W \cdot (m \cdot K)^{-1}$ is the thermal conductivity of oxygen-free copper tube in clean condition, and the heat transfer coefficient $K = 439.88 kW \cdot (m^2 \cdot K)^{-1}$ is calculated based on 12 mm outer diameter and 10 mm inner diameter of copper tube. The total heat transfer coefficient K' of the copper tube can be calculated according to Eq. 5 when considering the coating thermal resistance R_t and the fouling thermal resistance R_f .

$$K' = \frac{1}{\frac{1}{K} + R_t + R_f}. \quad (5)$$

Before calculating the thermal resistance of the coating and the thermal resistance of the dirt, the thermal conductivity of the OC sample surface calcium carbonate scale, the OC-WSR sample, and the OC-WSR-IF sample coating were measured by Hot Disk thermal constant analyzer and were $1.16 W \cdot (m \cdot K)^{-1}$, $2.59 W \cdot (m \cdot K)^{-1}$ and $18.44 W \cdot (m \cdot K)^{-1}$, respectively. Based on the measured results, it was clear that the low thermal conductivity of the OC-WSR sample coating was. The thermal conductivity mechanism of the coating is shown in Fig. 10, the OC-WSR sample coating material is an amorphous polymer, which lacks both free electrons and a complete lattice structure, and when the heat reaches its surface, it causes random vibration and rotation of the internal atoms, followed by transfer to neighboring atoms, and so on. This random and slow heat transfer leads to low thermal conductivity [28]. In contrast, the thermal conductivity is significantly increased by adding inorganic fillers such as graphite and graphene to the coating. Because graphite is a crystalline mineral of carbonaceous elements, which can be regarded as two-dimensional graphene molecules stacked in layers, its electrical conductivity and lattice structure are complete, with thermal conductivity of $129 W \cdot (m \cdot K)^{-1}$; the carbon atoms in graphene and the three surrounding carbon atoms undergo sp^2 hybridization to form σ -bonds, giving graphene a complete lattice structure, which relies on the non-simple harmonic vibrations of the elastic lattice (i.e., phonon

interactions) to transfer heat, and the thermal conductivity of a single layer of graphene can reach $5300 W \cdot (m \cdot K)^{-1}$. The introduction of an ordered carbon structure in the coating reduces the phonon scattering caused by the disordered and chaotic arrangement of macromolecules and promotes local order at the molecular level, while its reticular structure has a large specific surface area, allowing a smaller amount of carbon filler to form an excellent thermal conductivity network [29].

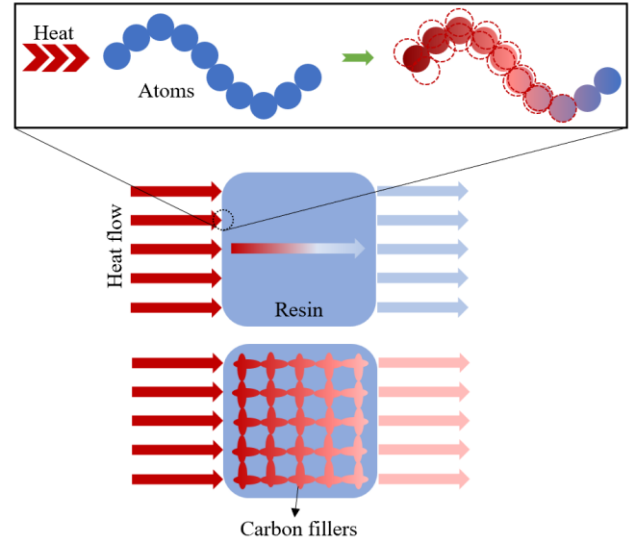


Fig. 10. Thermal conductivity mechanism of the coating

In the anti-fouling performance test, the amount of fouling on the surface of the OC sample varied at different locations, with the thickness of the scale layer ranging from $1 \mu m$ to $5 \mu m$, while the maximum thickness of the scale layer on the surface of the OC-WSR sample and the OC-WSR-IF sample was $2 \mu m$ and $0.5 \mu m$, respectively. The effects of copper tube fouling and surface coating on the total heat transfer coefficient of copper tubes are shown in Table 4. As can be seen from Table 4, the total heat transfer coefficient of the copper tube decreased rapidly as the thickness of the scale layer increased. When the thickness of the scale layer reached $5 \mu m$, the total heat transfer coefficient was only 34.53 % of that of the clean copper tube, indicating that the fouling seriously affected the heat transfer of the copper tube, resulting in a large amount of energy loss in practical applications. The surface coating of both the OC-WSR sample and OC-WSR-IF sample played a role in inhibiting the growth of fouling.

Table 4. Effect of fouling and coating on the total heat transfer coefficient of copper tube

样品	$\delta_f, \mu m$	$\lambda_f, W \cdot (m \cdot K)^{-1}$	$R_f, 10^{-6}(m^2 \cdot K) \cdot W^{-1}$	$\delta_t, \mu m$	$\lambda_t, W \cdot (m \cdot K)^{-1}$	$R_t, 10^{-6}(m^2 \cdot K) \cdot W^{-1}$	$K', kW \cdot (m^2 \cdot K)^{-1}$
OC	0	1.16	0	/	/	/	439.88
	1		0.8621				318.94
	2		1.7241				250.16
	3		2.5862				205.78
	4		3.4483				174.78
	5		4.3103				151.89
OC-WSR	2		1.7241	10	2.59	3.8160	127.25
OC-WSR-IF	0.5		0.4310	10	18.44	0.5423	308.01

However, the thermal conductivity of the OC-WSR sample surface coating was poor, and the total heat transfer coefficient after surface modification still decreased relative to the copper tube at 5 μm of fouling, which didn't have the potential for practical application. For the OC-WSR-IF sample surface coating, the overall heat transfer performance was still better than that of the uncoated scaled copper tube when the thermal resistance of the fouling and the thermal resistance of the coating were taken into account. Moreover, the total heat transfer coefficient was improved by 49.68 % relative to the copper tube with an average fouling thickness of 3 μm . Therefore, the coating is of great significance in the practical application for the continuous and efficient operation of gas water heaters and the extension of their service life.

3.5. Limitations analysis

Although this study has achieved some ideal results, there is still some content to be further improved, in the future work, can be aimed at the following content for more in-depth and systematic research. Firstly, this paper mainly studied the various properties of the coating, and the mechanism of the coating is still shallow, the later research can be an in-depth analysis of the coating of the corrosion resistance and anti-fouling mechanism. Next, the results in the paper are based on small sample experiments, to make the experimental results closer to the application in the heat exchanger, the later research can design a pipeline simulation experimental device, to get the comprehensive performance of the coating in the inner wall of the copper pipe, and the experimental results of this paper for comparison, to promote the practical application of the coating.

4. CONCLUSIONS

Three material surface samples of OC, OC-WSR, and OC-WSR-IF were prepared. The surface characterization, strength properties, corrosion, and fouling behavior of the three samples were investigated. The heat transfer performance of the samples under practical applications was analyzed, and the following conclusions were obtained:

1. The coating changed the wetting characteristics of OC samples, while its surface energy was reduced by 42.35 % – 82.40 %.
2. The wet adhesion reduction rate of OC-WSR samples was 0.1425 $\text{MPa}\cdot\text{d}^{-1}$. The addition of silicon carbide and graphite to the coating effectively slowed down the wet adhesion reduction rate, and the reduction rate was relatively minimal at 0.0375 $\text{MPa}\cdot\text{d}^{-1}$ at a silicon carbide to graphite mass ratio of 2:3. In addition, the coating has excellent wear resistance with the synergistic effect of silicon carbide and graphite.
3. Compared with the other two samples, the OC-WSR-IF sample has excellent corrosion and fouling resistance. In the most corrosive sulfuric acid solution, the corrosion rate was only $3.24 \times 10^{-2} \text{ mg}\cdot(\text{cm}^2\cdot\text{h})^{-1}$; the ratio of fouling induction period time was 1:1.86:2.43, the ratio of the maximum fouling amount of CaCO_3 was 6.25:2.60:1, and the ratio of average fouling rate in growth period was 7.02:2.47:1 after 492 h of dynamic fouling for the three samples.

4. Fouling seriously weakens the heat transfer performance of the copper tube, while the coating of high thermal conductivity not only inhibits the growth of fouling but also reduces the impact of the total heat transfer coefficient of the copper tube due to the thermal resistance of its coating, which increases the total heat transfer coefficient by 49.68 % compared to the fouling copper tube and has the potential for practical application.

Acknowledgments

This work was supported by National Key R&D Program of China(2020YFC1910100) and the Fundamental Research Funds for the Central Universities (10002150058).

REFERENCES

1. **Lebel, E.D., Lu, H.S., Speizer, S.A., Finnegan, C.J., Jackson, R.B.** Quantifying Methane Emissions from Natural Gas Water Heaters *Environmental Science & Technology* 54 (9) 2022: pp. 5737 – 5745. <https://doi.org/10.1021/acs.est.9b07189>
2. **Zhan, X.Y., Chen, Z.G., Qin, C.K.** Effect of Hydrogen-Blended Natural Gas on Combustion Stability and Emission of Water Heater Burner *Case Studies in Thermal Engineering* 37 2022: pp. 102246. <https://doi.org/10.1016/j.csite.2022.102246>
3. **Pantazopoulos, G., Tsinopoulos, G.** Corrosion of a Copper U-Shaped Heating Element: Some Morphological and Microstructural Observations *Journal of Failure Analysis and Prevention* 6 (6) 2006: pp. 8 – 12. <http://dx.doi.org/10.1361/154770206X156204>
4. **Kuźnicka, B.** Erosion–Corrosion of Heat Exchanger Tubes *Engineering Failure Analysis* 16 (7) 2009: pp. 2382 – 2387. <https://doi.org/10.1016/j.engfailanal.2009.03.026>
5. **Mohammadi, Z., Rahsepar, M.** The Use of Green Bistorta Officinalis Extract for Effective Inhibition of Corrosion and Scale Formation Problems in Cooling Water System *Journal of Alloys and Compounds* 770 (5) 2019: pp. 669 – 678. <https://doi.org/10.1016/j.jallcom.2018.08.198>
6. **Long, W., Wang, X., Hu, H., Lu, W., Liu, L., Zhou, M.P., Cao, S.R., Chen, X.W.** Primary Corrosion Cause of P110S Steel Tubing Corrosion Thinning in $\text{CO}_2\text{-H}_2\text{S}$ Well and Its Remaining Life Prediction *Processes* 11 (2) 2023: pp. 333. <https://doi.org/10.3390/pr11020333>
7. **Qiu, X.W., Zhang, Y.P., He, L., Liu, C.G.** Microstructure and Corrosion Resistance of AlCrFeCuCo High Entropy Alloy *Journal of Alloys and Compounds* 549 (5) 2013: pp. 195 – 199. <https://doi.org/10.1016/j.jallcom.2012.09.091>
8. **Karki, V., Singh, M.** Investigation of Corrosion Mechanism in Type 304 Stainless Steel under Different Corrosive Environments: A SIMS Study *International Journal of Mass Spectrometry* 421 2017: pp. 51 – 60. <https://doi.org/10.1016/j.ijms.2017.06.001>
9. **Close, D., Stein, N., Allain, N., Tidu, A., Drynski, E., Merklein, M., Lallement, R.** Electrodeposition, Microstructural Characterization and Anticorrosive Properties of Zn-Mn Alloy Coatings from Acidic Chloride Electrolyte Containing 4-Hydroxybenzaldehyde and Ammonium Thiocyanate *Surface and Coatings Technology* 298 (25) 2016: pp. 73 – 82. <https://doi.org/10.1016/j.surfcoat.2016.04.043>

10. Cui, M., Ren, S., Qin, S., Xue, Q., Zhao, H., Wang, L. Processable Poly(2-Butylaniline)/Hexagonal Boron Nitride Nanohybrids for Synergetic Anticorrosive Reinforcement of Epoxy Coating *Corrosion Science* 131 2018: pp. 187–198. <https://doi.org/10.1016/j.corsci.2017.11.022>
11. Zhang, T., Wang, Y., Chen, X., Hu, G., Meng, J., Wang, S. Bio-Inspired Superhydrophilic Coatings with High Anti-Adhesion Against Mineral Scales *NPG Asia Materials* 10 (3) 2018: pp. e471. <https://doi.org/10.1038/am.2017.224>
12. Qing, Y.Q., Yang, C.N., Sun, Y.Z., Zheng, Y.S., Wang, X.D., Shang, Y., Wang, L.S., Liu, C.S. Facile Fabrication of Superhydrophobic Surfaces with Corrosion Resistance by Nanocomposite Coating of TiO₂ and Polydimethylsiloxane *Colloids and Surfaces A: Physicochemical and Engineering Aspects* 484 (5) 2015: pp. 471–477. <https://doi.org/10.1016/j.colsurfa.2015.08.024>
13. Jiang, W., He, J., Xiao, F., Yuan, S.J., Lu, H.F., Liang, B. Preparation and Antiscalming Application of Superhydrophobic Anodized CuO Nanowire Surfaces *Industrial & Engineering Chemistry Research* 54 (27) 2015: pp. 6874–6883. <https://doi.org/10.1021/acs.iecr.5b00444>
14. Hu, K., Xu, Q.X., Yang X.L. Fabrication of Superhydrophobic Surfaces on Copper Substrates via Brush Plating Technique *Advanced Materials Research* 834–836 2014: pp. 662–669. <https://doi.org/10.4028/www.scientific.net/AMR.834-836.662>
15. Lee, C.Y., Zhang, B.J., Park, J., Kim, K.J. Water Droplet Evaporation on Cu-Based Hydrophobic Surfaces with Nano- and Micro-Structures *International Journal of Heat and Mass Transfer* 55 (7–8) 2012: pp. 2151–2159. <https://doi.org/10.1016/j.ijheatmasstransfer.2011.12.019>
16. Yu, D., Tian, J. Superhydrophobicity: Is It Really Better than Hydrophobicity on Anti-Corrosion? *Colloids and Surfaces A: Physicochemical and Engineering Aspects* 445 (20) 2014: pp. 75–78. <https://doi.org/10.1016/j.colsurfa.2014.01.016>
17. Oliveira, R. Understanding Adhesion: A Means for Preventing Fouling *Experimental Thermal and Fluid Science* 14 (4) 1997: pp. 316–322. [https://doi.org/10.1016/S0894-1777\(96\)00134-3](https://doi.org/10.1016/S0894-1777(96)00134-3)
18. Zou, H.L., Lin, S.D., Tu, Y.Y., Liu, G.J., Hu, J.W., Li, F., Miao, L., Zhang, G.W., Luo, H.S., Liu, F., Hou, C.M., Hu, M.L. Simple Approach Towards Fabrication of Highly Durable and Robust Superhydrophobic Cotton Fabric from Functional Diblock Copolymer *Journal of Materials Chemistry A* 1 (37) 2013: pp. 11246–11260. <https://doi.org/10.1039/C3TA12224G>
19. Li, S., Wang, D., Xiao, H., Zhang, H., Cao, S.L., Chen, L.H., Ni, Y.H., Huang, L.L. Ultra-low Pressure Cellulose-Based Nanofiltration Membrane Fabricated on Layer-By-Layer Assembly for Efficient Sodium Chloride Removal *Carbohydrate Polymers* 255 (1) 2021: pp. 117532. <https://doi.org/10.1016/j.carbpol.2020.117532>
20. Qian, H.J., Zhu, M.L., Song, H., Wang, H.Y., Liu, Z.J., Wang, C.J. Anti-Scaling of Superhydrophobic Poly(Vinylidene Fluoride) Composite Coating: Tackling Effect of Carbon Nanotubes *Progress in Organic Coatings* 142 2020: pp. 105566. <https://doi.org/10.1016/j.porgcoat.2020.105566>
21. Qian, H.J., Zhu, Y.J., Wang, H.Y., Song, H., Wang, C.J., Liu, Z.J., Li, H.W. Preparation and Anti-Scaling Performance of Superhydrophobic PPS/PTFE Composite Coating *Industrial & Engineering Chemistry Research* 56 (44) 2017: pp. 12663–12671. <https://doi.org/10.1021/acs.iecr.7b03975>
22. Shi, Z.Y., Liu, Z.Q., Song, H., Zhang, X.Z. Prediction of Contact Angle for Hydrophobic Surface Fabricated with Micro-Machining Based on Minimum Gibbs Free Energy *Applied Surface Science* 364 (28) 2016: pp. 597–603. <https://doi.org/10.1016/j.apsusc.2015.12.199>
23. Owens, D.K., Wendt, R.C. Estimation of the Surface Free Energy of Polymers *Journal of Applied Polymer Science* 13 (8) 1969: pp. 1741–1747. <https://doi.org/10.1002/app.1969.070130815>
24. Liu, L.J., Liu, W.K., Chen, R.F., Li, X., Xie, X.J. Hierarchical Growth of Cu Zigzag Microstrips on Cu Foil for Superhydrophobicity and Corrosion Resistance *Chemical Engineering Journal* 281 (1) 2015: pp. 804–812. <https://doi.org/10.1016/j.cej.2015.07.028>
25. Ren, L., Cheng, Y.H., Yang, J.Y., Wang, Q.G. Study on Heat Transfer Performance and Anti-Fouling Mechanism of Ternary Ni-W-P Coating *Applied Science* 10 (11) 2020: pp. 3905. <https://doi.org/10.3390/app10113905>
26. Wu, Z., Davidson, J.H., Francis, L.F. Effect of Water Chemistry on Calcium Carbonate Deposition on Metal and Polymer Surfaces *Journal of Colloid and Interface Science* 343 (1) 2010: pp. 176–187. <https://doi.org/10.1016/j.jcis.2009.11.031>
27. Choi, C.H., Kim, C.J. Large Slip of Aqueous Liquid Flow over a Nanoengineered Superhydrophobic Surface *Physical Review Letters* 96 (6) 2006: pp. 066001-1–066001-4. <https://doi.org/10.1103/physrevlett.96.066001>
28. Yang, X.T., Liang, C.B., Ma, T.B., Guo, Y.Q., Kong, J., Gu, J.W., Chen, M.J., Zhu, J.H. A Review on Thermally Conductive Polymeric Composites: Classification, Measurement, Model and Equations, Mechanism and Fabrication Methods *Advanced Composites and Hybrid Materials* 1 2018: pp. 207–230. <http://dx.doi.org/10.1007/s42114-018-0031-8>
29. Novoselov, K.S., Jiang, D., Schedin, F., Booth, T.J., Khotkevich, V.V., Morozov, S.V., Geim, A.K. Two-Dimensional Atomic Crystals *Proceedings of the National Academy of Sciences* 102 (30) 2005: pp. 10451–10453. <https://doi.org/10.1073/pnas.0502848102>



© Wang et al. 2024 Open Access This article is distributed under the terms of the Creative Commons Attribution 4.0 International License (<http://creativecommons.org/licenses/by/4.0/>), which permits unrestricted use, distribution, and reproduction in any medium, provided you give appropriate credit to the original author(s) and the source, provide a link to the Creative Commons license, and indicate if changes were made.